

# Lower-order-symmetry induced bandwidth-controllable terahertz polarization converter

XiaoFei Zang<sup>1,2</sup>, Suji Liu<sup>1</sup>, QingQing Cheng<sup>1,2</sup>, JingYa Xie<sup>1,2</sup>,  
YiMing Zhu<sup>1,2</sup> and YaJun Wang<sup>3</sup>

<sup>1</sup>Shanghai Key Lab of Modern Optical System, University of Shanghai for Science and Technology, Shanghai 200093, People's Republic of China

<sup>2</sup>Terahertz Science Cooperative Innovation Center, Chengdu 610054, People's Republic of China

<sup>3</sup>North Electro-Optics Group Co., LTD, Dian Zi San Lu Road, No. 9, Yanta District, Xi'an, 710065, People's Republic of China

E-mail: [ymzhu@usst.edu.cn](mailto:ymzhu@usst.edu.cn)

Received 13 May 2017, revised 1 September 2017

Accepted for publication 11 September 2017

Published 13 October 2017



CrossMark

## Abstract

A transmission-type terahertz (THz) variable-bandwidth cross-polarization converter consisting of single-layer ultrathin metasurface is designed, fabricated and experimentally demonstrated. Both the simulated and measured results show that the bandwidth of linear polarization conversion is about 0.45 THz with a polarization conversion ratio over 90%. Different from the previous studies that mainly contributed to the geometry phase, the excellent characteristic of our designed device results from field-suppression of co-polarization components and field-enhancement of cross-polarization components, respectively. Even more intriguingly, the bandwidth of cross-polarization conversion is tunable by consecutively breaking the symmetry of the micro-structure, that is, the lower-order rotational symmetry, leading to a lower-order-symmetry-controlled THz cross-polarization conversion. Our study is an important step forward in developing compact, integrated, and bandwidth-controllable THz circuits and functional devices.

Keywords: ultrathin metasurface, polarization converter, bandwidth-controllable

(Some figures may appear in colour only in the online journal)

## 1. Introduction

Transformation optics, proposed by U. Terahertz (THz) waves, defined as 0.1–10 THz (10<sup>12</sup> cycles per second), have attracted much attention due to their potential applications in noninvasive testing, chemical and biological sensing, wireless communication, and so on [1–4]. However, most existing THz components such as THz sources, detectors, modulators, filters, sensors, absorbers and polarizations, are still large and bulky, which hinder the large-scale integration of THz system [5]. As a consequence, some new possible technologies (such as metamaterial technology and photonic crystal) are developed to resolve these issues. Metasurfaces are metamaterials of reduced dimensionality, which open up new avenues for designing the ultra-compact THz devices with low cost fabrication and reduced absorption due to their unique way of manipulating electromagnetic (EM) wavefront at subwavelength scale [6, 7].

Many metasurface-based ultra-thin devices with innovative functionalities, such as a generalized Snell's law of refraction, dual-polarity planar metalens, spin-Hall effect, wave plates, holograms and vortex beam, were proposed and demonstrated [8–15].

Polarization conversion devices that convert a beam of EM waves into a well-defined polarization state, have wide applications in THz science and technology such as imaging, detection, sensing, signal processing, etc. Recently, metasurfaces have been utilized to realize the ultra-compact and high-efficiency polarization conversion devices. For example, Hao *et al.*, proposed a reflection-type metasurface to manipulate the polarization state of incident beams based on the anisotropic characteristics of the *H*-shaped micro-structure [16]. Li *et al.*, and Levesque *et al.*, have proposed L-shaped nanostructure to realize single-frequency and narrow-band cross-polarization of reflected waves by using charge transfer

in the corner of the designed structure [17, 18]. At the same time, high-efficiency and broadband (reflection-type) linear-polarization converters (LPCs) were demonstrated by virtue of the multi-frequency superposition or the half-wave plate effects induced by the geometry phase [19–23]. Furthermore, Sui *et al* demonstrated the synthesis topology optimization method to design ultra-broadband LPCs [24]. Then, a theoretical work of broadband tunable (reflection-type) LPC based on graphene-based metasurfaces was also reported by controlling the Fermi energy of the graphene sheets [25]. Besides the reflection-type polarization conversion devices, polarization conversion in transmission mode has also aroused considerable attention. For instance, based on the multi wave interference effects, tri-layer grating metasurfaces were designed by Cong *et al* to freely rotate the linear polarization of THz waves in a broadband configuration [26, 27]. Another method to realize polarization rotation in transmission mode is based on the contribution of the localized surface plasmons (LSP) and surface plasmon polaritons [28]. Moreover, rotationally symmetric ‘F’ shaped and cavity-based transmission-type LPCs were theoretical designed and experimentally demonstrated, respectively [29, 30]. In addition to the LPCs, other kinds of single-frequency, multi-frequency and broadband metasurface-based linear-to-circular polarization converters have also been widely investigated ranging from microwave to optical frequencies by a similar approach [31–38].

To date, most of the LPCs mainly rely on the reflection-mode, resulting in the inherent challenge in separating the reflected wave from the incident wave. In addition, the physical mechanism of the metasurface-based LPCs [19–23] is attributed to the geometry phase (due to the rotation of the nano-pillars). More importantly, how to control the bandwidth of LPC have not been drawn sufficient attentions until now. In this paper, we propose and experimentally demonstrate a single-layer THz broadband cross-polarization converter in transmission mode by breaking the symmetry of the designed structure (double-split air ring micro-structure). For the incident THz waves with horizontal polarization, the excited  $E_x$  components in horizontal direction are cancelled out due to the  $\pi$  phase difference between them, while maintaining the orthogonal  $E_y$  components with phase changing of 0, leading to a nearly  $90^\circ$  rotation of the transmitted THz waves. In particular, the bandwidth of our proposed device can be well manipulated by gradually breaking the symmetry of the micro-structure, acting as a bandwidth-controllable THz cross-polarization converter. We also noted that a double-split metal ring micro-structure was proposed to achieve a giant amplitude modulation and the polarization conversion (just in single-frequency with the maximum PCR about 60%) based on the reduced coupling of the metamaterial structure with the free space and the constructive resonance in the direction of the incident electric field (co-polarization direction) [39]. Here, we design a Babynet metasurface (a complementary structure) to mainly discuss a broadband (with the maximum bandwidth of 0.45 THz), especially a bandwidth-controllable LPC with PCR over 90%. The fundamental principal (polarization conversion) of such

a structure mainly contributes to the field-suppression of co-polarization components (destructive resonance in co-polarization direction) and field-enhancement of cross-polarization components (constructive resonance in cross-polarization direction).

## 2. Design and fabrication

Figure 1 illustrates the schematics and optical images of such a lower-order-symmetry-controlled broadband THz polarization converter. The Babynet-inverted resonator arrays (metasurfaces) is designed as shown in figures 1(a) and (b) (unit cell), which consists of split dual-ring air slots embedded in the gold film. For  $\Delta S_1 = \Delta S_2 = 0$  (figure 1(b)), the planar metasurfaces are symmetrical in both  $x$ - and  $y$ -axis, resulting in non-polarization rotation or conversion. However, for  $\Delta S_1 = \Delta S_2 \neq 0$ , the structure symmetry is broken in both  $x$ - and  $y$ -axis, i.e., the two-fold rotational symmetry (the lowest order rotational symmetry). In this situation, the cross-polarization ( $y$ -polarized) transmission THz waves are observed (red arrows in figure 1(a)) for the  $x$ -polarized illumination. More interesting is that the bandwidth of cross-polarization conversion can be well modulated by gradually varying  $\Delta S_1$  ( $\Delta S_2$ ), that is, consecutive shifting of both the metal rods (the region in the dashed box). The detailed structure parameters are as follows:  $L_1 = 70 \mu\text{m}$ ,  $L_2 = 110 \mu\text{m}$ ,  $P = 180 \mu\text{m}$ ,  $L_{3+} L_4 + h = 90 \mu\text{m}$  ( $L_3' + L_4' + h = 90 \mu\text{m}$ ,  $L_3, L_3', L_4, L_4'$ , and  $h$  are variables), and  $\Delta S_1 = \Delta S_2$ . The thickness of the gold film is 100 nm with electrical conductivity of  $4.561 \times 10^7 \text{ s m}^{-1}$ . The substrate is polyimide (PI) with thickness of  $25 \mu\text{m}$ , and the corresponding permittivity is  $\varepsilon_{\text{pi}} = 3.5 + 0.035i$ . To experimentally demonstrate the broadband and bandwidth-controllable linear polarization conversion, the ultra-thin metasurfaces were fabricated using the standard photolithography process and the lift-off process. After a serial of technical processing such as spin-coating, photolithography, sputtering, and lift-off, the two-fold rotational symmetry of metasurfaces are formed on the PI substrate, as shown in figures 1(c) and (d).

## 3. Results

The polarization characteristics of the transmitted THz waves can be described by the polarization conversion rate (PCR), which is defined as

$$\text{PCR} = t_{yx}^2 / (t_{xx}^2 + t_{yx}^2),$$

where  $t_{ij}$  is the  $i$ -polarized electric-field component transmission from  $j$ -polarized incident THz waves ( $i, j = x, y$ ). In this paper, the polarization of the incident THz waves is  $x$ -polarized in all of the simulations and measurements.

Figure 2 shows bandwidth-controllable properties of such a linear polarization converter by changing of the  $\Delta S$  ( $\Delta S_1 = \Delta S_2 = \Delta S$ ), i.e., gradual symmetry breaking in the split dual-ring slots, with  $L_3 = L_3' = 31 \mu\text{m}$ ,  $L_4 = L_4' = 27 \mu\text{m}$ ,  $h = 32 \mu\text{m}$ . Here, the simulations of the

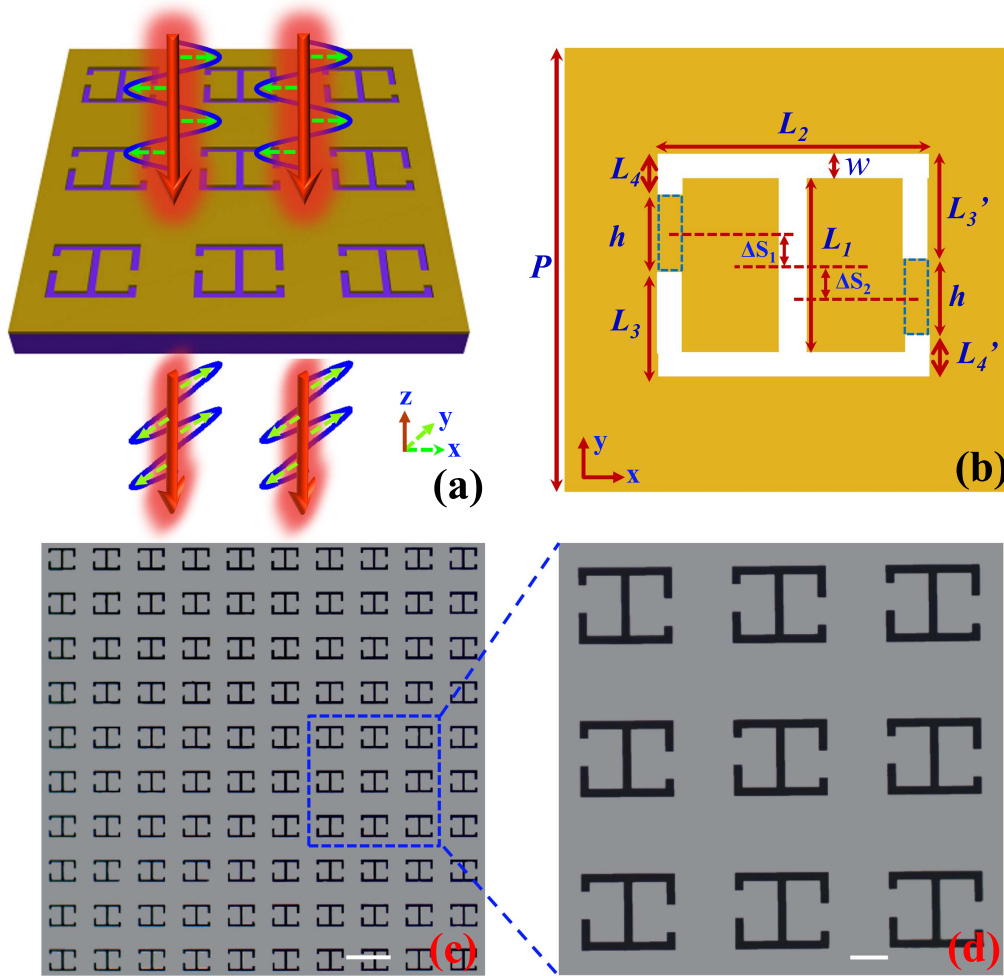


**Figure 1.** Schematics illustrating the periodical structure (a) and unit cell (b) of the broadband terahertz linear polarization converter. (c), (d) Optical images of one part of the fabricated sample. The scales in (c) and (d) are 200  $\mu\text{m}$  and 50  $\mu\text{m}$ , respectively.

transmittance spectra and PCR are carried out by the commercial microwave software CST Microwave Studio<sup>®</sup>. And, the THz time domain spectroscopy (THz-TDS) system with 9.5 GHz resolution is utilized to measure the corresponding transmittance spectra of the sample. For  $\Delta S_1 = \Delta S_2 = 14 \mu\text{m}$  and  $x$ -polarized illumination, as shown in figure 2(a<sub>1</sub>), the transmittance of the cross-polarized THz waves ( $t_{yx}$ ) is much higher than that of the co-polarized component ( $t_{xx}$ ) ranging from 0.61 to 1.06 THz, which means that the polarization of the transmitted THz wave is mainly converted into their perpendicular direction (cross-polarization). Therefore, a broadband (0.45 THz) cross-polarization converter is realized with PCR over 90%, as shown in figure 2(a<sub>2</sub>). Comparing with the calculated and measured results, they show good agreement, except for a slight frequency shift between them. This discrepancy is attributed to the fabrication errors. On the other hand, for  $\Delta S_1 = \Delta S_2 = 0$ , the PCR is nearly zero ranging from 0.35 to 1.45 THz (not show here), resulting in the non-cross-polarized transmitted THz waves. That is to say, there will be no polarization rotation in the case of the micro-structure with symmetry both in  $x$ - and  $y$ -axis. On the contrary, when  $\Delta S_1 = \Delta S_2 \neq 0$  (i.e.  $\Delta S_1 = \Delta S_2 = 14 \mu\text{m}$ ), the

metasurfaces show asymmetry both in  $x$ - and  $y$ -axis, and the PCR over 90% appears at  $f = 0.61\text{--}1.06$  THz in both simulation and measurement. Here, we emphasize that although the metasurfaces present asymmetrical in  $x$ - and  $y$ -axis directions for  $\Delta S_1 = \Delta S_2 \neq 0$ , the designed micro-structure still has two-fold rotational symmetry, which can be defined as the lowest order rotational symmetry. Therefore, the cross-polarized conversion of transmitted THz waves is completely demonstrated by the asymmetrical (lower-order-symmetry) of the metasurfaces. When we further decrease the shifting distance of the metal rods (the region in the dashed box of figure 1(b)) i.e.,  $\Delta S = 8 \mu\text{m}, 4 \mu\text{m}$ , the measured PCR over 90% are 0.24 THz and 0.14 THz, respectively, as shown in figures 2(b<sub>2</sub>) and (b<sub>3</sub>) of the gray regions (the transmittance spectra are shown in figures 2(a<sub>2</sub>) and (a<sub>3</sub>)), which demonstrates that the bandwidth (with PCR over 90%) of our designed linear polarization converter can be well modulated by accurately controlling the shifting distance of metal rods. Figure 2(c) shows the numerical simulation of PCR versus gradual change of the shifting distance  $\Delta S$ , which further verifies the controllable bandwidth of the broadband cross-polarized conversion.

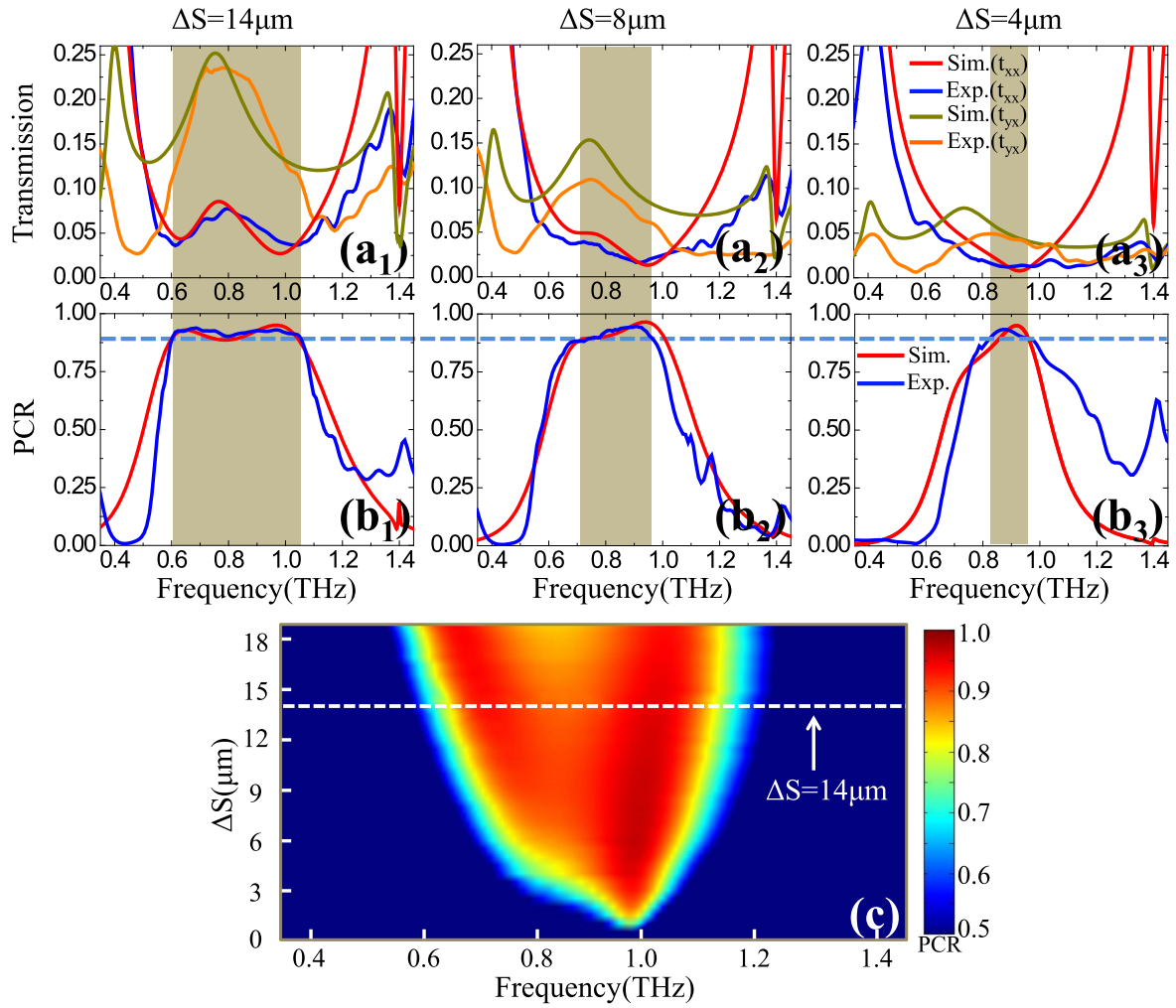


**Figure 2.** Simulated and measured transmittance spectra and PCR for  $\Delta S_1 = \Delta S_2 = 14 \mu\text{m}$  (a<sub>1</sub>) and (b<sub>1</sub>),  $\Delta S_1 = \Delta S_2 = 8 \mu\text{m}$  (a<sub>2</sub>) and (b<sub>2</sub>),  $\Delta S_1 = \Delta S_2 = 4 \mu\text{m}$  (a<sub>3</sub>) and (b<sub>3</sub>) and  $h = 32 \mu\text{m}$ . (c) PCR with gradually varying the values of  $\Delta S$  ( $\Delta S_1 = \Delta S_2 = \Delta S$ ).

To understand the underlying mechanism of cross-polarized conversion caused by the asymmetric/lower-order-symmetry, electric-field and phase distributions at 0.65, 0.79, and 0.97 THz for  $\Delta S = 14 \mu\text{m}$  were numerically calculated shown in figure 3. Taking  $f = 0.79$  THz for example, the excited  $E_x$  field distributions are mainly located in the top left arm, the bottom right arm and the middle arm of air slots (figure 3(b<sub>1</sub>)) with the  $x$ -polarized normal illumination. Meanwhile, the cross-polarized component ( $E_y$ ) is also excited with the corresponding field distributions are located in the upper and the lower arm of air slots, as shown in figure 3 (b<sub>3</sub>). Here, the aggregation of the excited electric field in air slots is solely dependent on the shape of the slots, which can be considered as the LSPs [40]. The corresponding phase distribution for the excited co-polarized component ( $E_x$ ) is shown in figure 3(b<sub>2</sub>). We can find that the phase difference between the side and the middle arms is nearly  $\pi$ , which means that the electric fields in the side and middle air slots destructively interfere with each other, leading to nearly zero intensity in transmitted  $x$ -polarized THz waves at  $f = 0.91$  THz. On the contrary, the phase difference between  $E_y$  components is nearly 0 (figure 3(b<sub>4</sub>)), resulting in the high

transmission of the cross-polarized THz waves. In other words, by designing proper lower-order-symmetry structure, the  $E_x$  of LSPs can be approached to zero by virtue of the destructive interference (destructive resonance in co-polarization direction), meanwhile the excited  $E_y$  component still has zero phase difference (constructive resonance in co-polarization direction). Therefore, the main physical mechanism of the cross-polarization conversion for our designed devices is field-suppression of the co-polarization components and field-enhancement of the cross-polarization components. Obviously, for  $x$ -polarized incident THz waves and  $f = 0.65, 0.98$  THz, both of the co-polarized and cross-polarized transmitted THz waves are also excited at these two separated frequencies. However, the co-polarized THz waves are nearly cancelled out due to the nearly  $\pi$ -phase-difference between the side and the middle arms as depicted in figures 3 (a<sub>2</sub>) and (c<sub>2</sub>), while the cross-polarized THz waves are maintained with high-transmittance because of the 0-phase-difference between  $E_y$  (cross-polarized) components (figures 3(a<sub>3</sub>), (c<sub>3</sub>) and (a<sub>4</sub>), (c<sub>4</sub>)), demonstrating a broadband of LPC. On the other hand, by gradually decreasing the shifting distance of the metal rods, the response bandwidth of

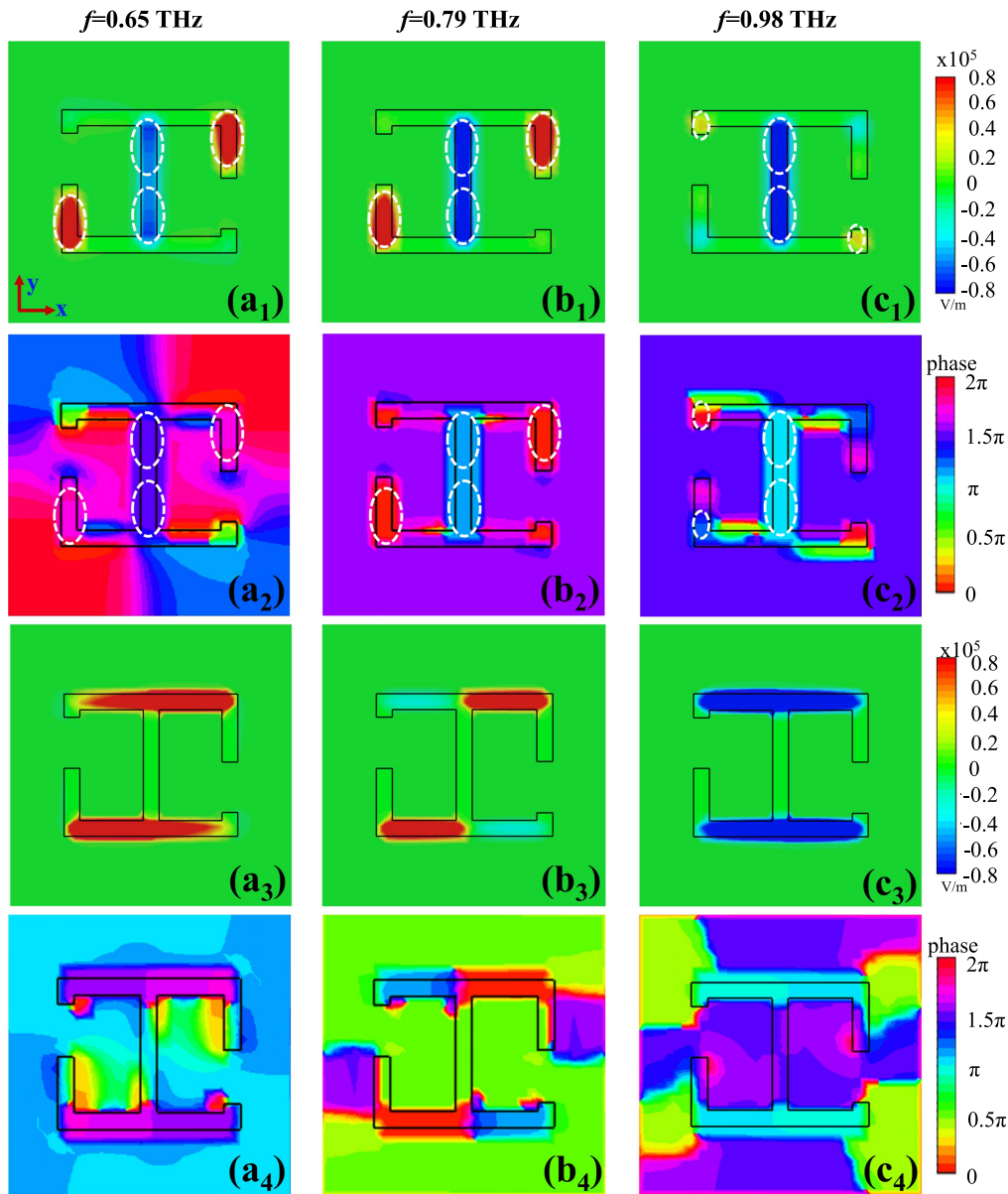


**Figure 3.** Simulated electric field and phase distributions for  $\Delta S = 14 \mu\text{m}$  at 0.65, 0.79, and 0.97 THz. (a<sub>1</sub>)–(c<sub>1</sub>) The electric field distributions of the excited  $x$ -component ( $E_x$ ). (a<sub>2</sub>)–(c<sub>2</sub>) The corresponding phase distributions of the electric field (in (a<sub>1</sub>)–(c<sub>1</sub>)) for the excited  $x$ -component. (a<sub>3</sub>)–(c<sub>3</sub>) The electric field distributions of the excited  $y$ -component ( $E_y$ ). (a<sub>4</sub>)–(c<sub>4</sub>) The corresponding phase distributions of the electric field (in (a<sub>3</sub>)–(c<sub>3</sub>)) for the excited  $y$ -component.

the destructive resonance in co-polarization direction is also decreased. Therefore, the bandwidth-controllable LPC can be realized by manipulating the shifting distance of the metal rods (see figures 2(b<sub>1</sub>) and (b<sub>3</sub>)).

When we consecutively break the symmetry of the microstructure, the bandwidth (with PCR > 90%) is gradually enhanced, leading to the bandwidth-controllable polarization converter. Therefore, the tunable (bandwidth-controllable) physical mechanism is that the PCR maintains more than 90% in a broader region when we increase the parameter  $\Delta S$ . Now, we give the detailed physical interpretation as follows:

Taking  $f = 0.6 \text{ THz}$  for example. In this case, the PCR for  $\Delta S = 0, 4, 8, 14 \mu\text{m}$  are 0%, 50% and 90%, respectively. For  $\Delta S = 0$  and  $x$ -polarized incidence, the incident

electric field is mainly located in the middle arm (see figure 4 (a<sub>1</sub>)). Although the cross-polarized component is also excited in the bottom and up-arms (figure 4(a<sub>3</sub>)), it is cancelled out due to the destructive interference with  $\pi$  phase difference between these electric fields in the two arms (see the black dash box in figures 4(a<sub>3</sub>) and (a<sub>4</sub>)). Therefore, there is non-cross-polarized polarization conversion for  $\Delta S = 0$ . When  $\Delta S \neq 0$ , the  $x$ -component electric field is excited in the bottom left and upper right arms. The larger  $\Delta S$ , the stronger density of the excited  $x$ -component electric field (see figures 4 (b<sub>1</sub>) and (d<sub>1</sub>)). In addition, the phase difference between the excited electric field in the bottom left (or upper right) arms and the middle arm is nearly  $\pi$  (see figures 4(b<sub>2</sub>)–(d<sub>2</sub>)), resulting in destructive interference between them. However, for  $\Delta S = 4, 8 \mu\text{m}$ , the density of the excited  $x$ -component

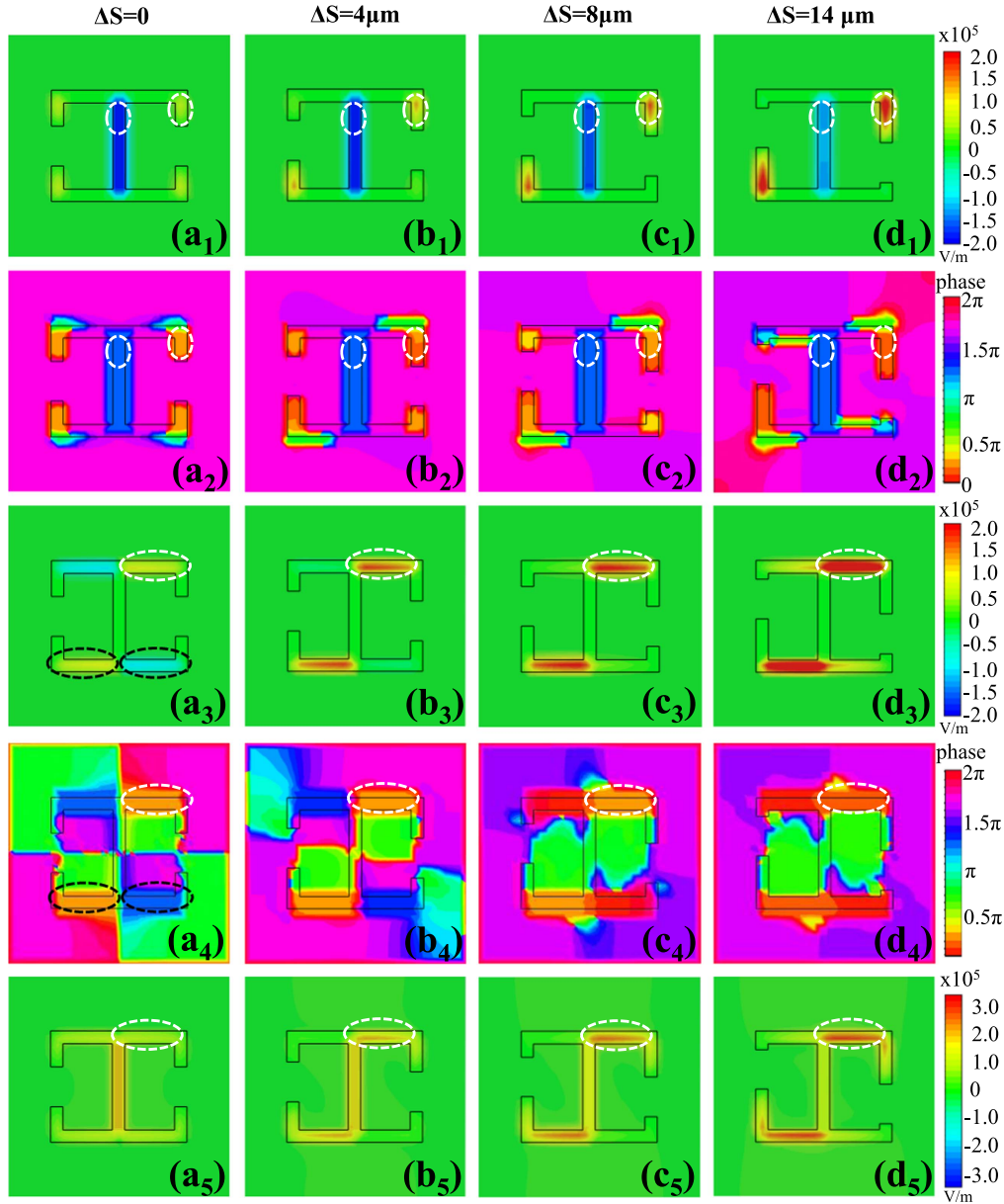


**Figure 4.** Simulated electric field, phase and E-field energy density distributions for  $\Delta S = 0, 4, 8, 14 \mu\text{m}$  at 0.6 THz (under the  $x$ -polarized incidence). (a<sub>1</sub>)–(d<sub>1</sub>) The electric field distributions of the excited  $x$ -component. (a<sub>2</sub>)–(d<sub>2</sub>) The corresponding phase distributions of the electric field for the excited  $x$ -component. (a<sub>3</sub>)–(d<sub>3</sub>) The electric field distributions of the excited  $y$ -component. (a<sub>4</sub>)–(d<sub>4</sub>) The corresponding phase distributions of the electric field for the excited  $y$ -component. (a<sub>5</sub>)–(d<sub>5</sub>) The corresponding electric field density distribution for  $\Delta S = 0, 4, 8, 14 \mu\text{m}$  at 0.6 THz, respectively.

electric field in both side (left and right) arms is not enough strong to cancel the corresponding electric field located in the middle arm. The  $x$ -component electric field can be cancelled out only when  $\Delta S = 14 \mu\text{m}$ . In a word, when we enhance the parameter  $\Delta S$ , the excited  $y$ -component (cross-polarized) electric field is become more and more strong located in upper and bottom arms, as shown in figures 4(a<sub>3</sub>)–(d<sub>3</sub>) (the corresponding phase distributions are shown in figures 4 (a<sub>4</sub>)–(d<sub>4</sub>)). Actually, the polarization conversion is related to the enhancement of the cross-polarization in  $y$ -component and reduction of the co-polarization in  $x$ -component for the

$x$ -polarized incidence. From the above discussion, it can be found that for  $\Delta S < 14 \mu\text{m}$ , i.e.  $\Delta S = 4, 8 \mu\text{m}$ , the  $x$ -component localized field is not cancelled out completely, while the excited  $y$ -component localized field is not so stronger, resulting in a low PCR (at  $\Delta S = 4, 8 \mu\text{m}$ ). In figures 4(a<sub>5</sub>)–(d<sub>5</sub>), with the enhancement of  $\Delta S$ , the corresponding electric field density is become more and more strong in the bottom and upper arms (cross-polarized electric field), while the electric field density is much more weak in the middle arm (co-polarized electric field), which demonstrate the energy conversion gradually from  $x$ -polarized THz

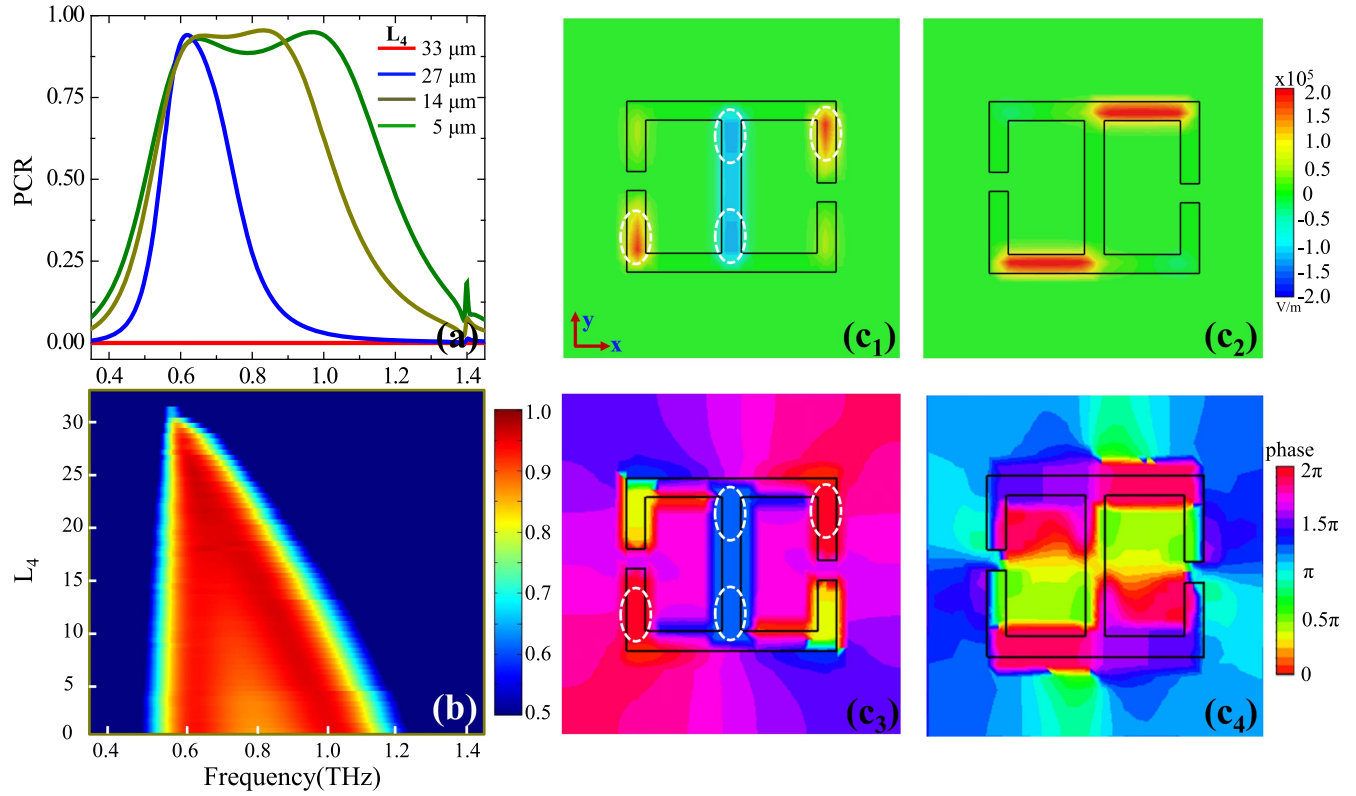


**Figure 5.** (a) PCR ( $L_4 = L'_4$ ) for  $L_4 = 33 \mu\text{m}$  (red line),  $27 \mu\text{m}$  (blue line),  $14 \mu\text{m}$  (dark yellow line),  $5 \mu\text{m}$  (green line). (b) PCR versus the varying of  $L_4$ . (c<sub>1</sub>)–(c<sub>2</sub>) The electric field distributions for of the excited  $x$ -component (left) and  $y$ -component (right), respectively, for  $L_4 = 27 \mu\text{m}$  at  $f = 0.61 \text{ THz}$ . (c<sub>3</sub>)–(c<sub>4</sub>) The corresponding phase distributions for the electric field distributions of the excited  $x$ -component (left) and  $y$ -component (right), respectively.

waves to the  $y$ -polarized THz waves (when we gradually increase  $\Delta S$ ). In other words, with increasing the structure  $\Delta S$ , the incident  $x$ -polarized field is gradually converted into the  $y$ -component (cross-polarized), leading to a broad bandwidth (with PCR > 90%) response for large  $\Delta S$ . Since a large  $\Delta S$  corresponding to a broad bandwidth (with PCR > 90%) response (in turn, a narrow bandwidth is corresponding to a small  $\Delta S$ ), we can tune the bandwidth by controlling the structure  $\Delta S$ .

The above investigation of manipulating bandwidth of the linear polarization converter is mainly dependent on the shifting of metal rods (with fixed length). Now, we propose another method to control the bandwidth of the cross-polarized conversion. Here, the length of  $L_3$  ( $L_3 = L'_3 = 33 \mu\text{m}$ ) is fixed, and we gradually change the length of  $L_4$  ( $L_4 = L'_4$ ), that is, modulating the length of metal rods, to achieve a bandwidth-controllable linear polarization converter, as shown in figures 5(a) and (b). For  $L_4 = 33, 27, 14$  and  $5 \mu\text{m}$ , the bandwidth of PCR over 90% is 0, 0.025, 0.3, and 0.45 THz, which means that the bandwidth of the cross-polarized conversion is gradually enhanced with decreasing the length ( $L_4$ ) of the upper left and lower right air slots (see figure 1(b)). In addition, the physical mechanism in this case is analogous to the analysis in the above. When  $L_4 = 27 \mu\text{m}$  and  $f = 0.61 \text{ THz}$ , the transmitted  $E_x$  field components are suppressed for the destructive interference, and the

corresponding  $E_y$  field components are enhanced for the in-phase transmission (see figures 5(c<sub>1</sub>)–(c<sub>4</sub>)).

#### 4. Discussion

We discuss the polarization conversion properties for the metal rods (the region in the dashed box of figure 1(b)) shifting in the same direction, as shown in the inset ( $I_1$ – $I_3$ ) of figure 6(a). For  $\Delta S \neq 0$ , the structure is asymmetrical in  $x$ -axis but symmetrical in  $y$ -axis. Figure 5(a) illustrates the PCR for  $\Delta S = 0, 9.5 \mu\text{m}, 19 \mu\text{m}$ , respectively. Now, it is quite different from the above case of breaking the symmetry in both  $x$ - and  $y$ -axis, that is, the cross-polarized conversion is nearly inexistent (figure 6(d)). In order to understand the physical original of the non-existence of cross-polarization conversion, we show the corresponding electric field and phase distribution for  $\Delta S = 9.5 \mu\text{m}$  at  $f = 0.825 \text{ THz}$ , as shown in figures 6(c<sub>1</sub>)–(c<sub>4</sub>). For the  $x$ -polarized illumination, both  $x$ -polarized and  $y$ -polarized transmitted THz waves are excited simultaneously (figures 6(c<sub>1</sub>)–(c<sub>2</sub>)). It should be noted that the electric field distributions of the excited cross-polarized ( $y$ -polarized) transmitted THz waves, located in these two white-dot-box regions, are almost symmetrical from each other but with phase difference of  $\pi$  (see figure 6(c<sub>4</sub>)), leading to a perfect destructive interference for  $E_y$  components. For the excited  $x$ -polarized transmitted THz waves, the electric

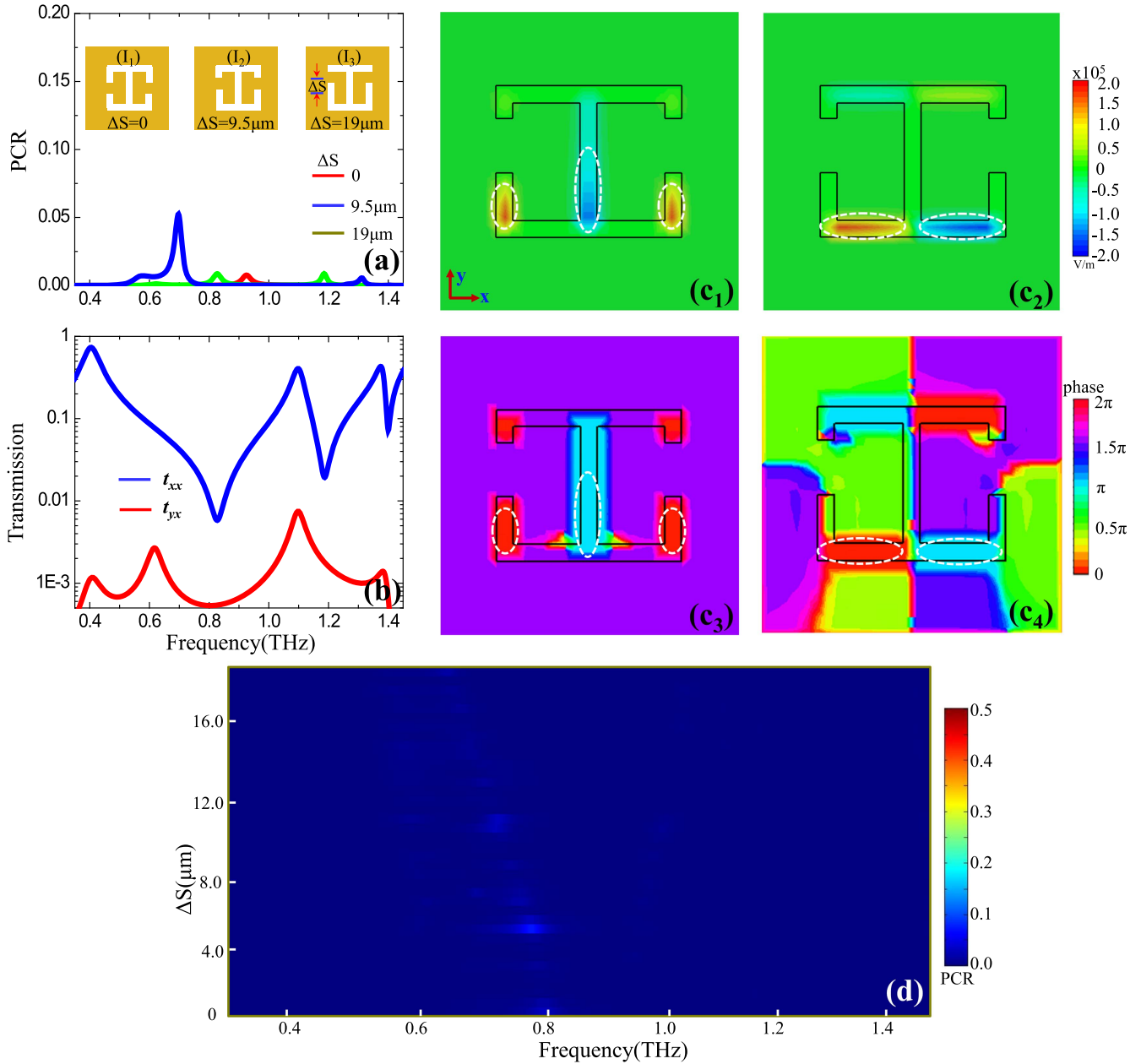


**Figure 6.** (a) PCR for  $\Delta S = 0$  (red line),  $9.5 \mu\text{m}$  (blue line),  $19 \mu\text{m}$  (dark yellow line); (b) the transmittance spectra for  $\Delta S = 9.5 \mu\text{m}$ ; (c<sub>1</sub>)–(c<sub>2</sub>) the electric field distributions for of the excited  $x$ -component (left) and  $y$ -component (right), respectively, for  $\Delta S = 9.5 \mu\text{m}$  and  $f = 0.825$  THz. (c<sub>3</sub>)–(c<sub>4</sub>) The corresponding phase distributions for the electric field distributions of the excited  $x$ -component (left) and  $y$ -component (right), respectively. Inset in (a):  $(I_1)$ – $(I_3)$  are the schematics of unit cell for the metal rods shifting in the same direction with  $\Delta S = 0, 9.5 \mu\text{m}$ , and  $19 \mu\text{m}$ , respectively. (d) PCR versus the varying of  $\Delta S$ .

fields located in the two side arms are also destructive interference with the electric fields located in the middle arm, but they cannot be totally cancelled out. The transmission spectra ranging from 0.35 to 1.45 THz (see figure 6(b)) also demonstrate that the transmitted  $y$ -electric component is very weak (nearly approached to zero), while the transmitted  $x$ -electric component plays a major role (which is larger than that of the transmitted  $y$ -electric component). Therefore, cross-polarization conversion will not be achieved in this case because of the perfect destructive interference of the excited  $E_y$  components.

Finally, we give an appropriate comparison between our device and the previously reported design in terms of the PCR, and bandwidth. In table 1, we show the comparison between our polarization converter and other reported designs relate to the PCR and bandwidth. From the comparison, we can find that the property (PCR and bandwidth) our proposed device is in the intermediate level among all of the previous works. However, we want to emphasize that the main innovation of our work is the bandwidth-controllable THz polarization converter, that is, we can manipulate the bandwidth of the THz polarization converter by consecutively breaking the

**Table 1.** A comparison between our polarization converter and other reported designs in term of the PCR and bandwidth.

| Literature                 | PCR   | Bandwidth        |
|----------------------------|-------|------------------|
| Hao et al (2007) [16]      | 100%  | single frequency |
| Li et al (2010) [17]       | 93%   | single frequency |
| Grady et al (2013) [19]    | >90%  | 1.07 THz         |
| Cong et al (2013) [26]     | ≈100% | 0.61 THz         |
| Levesque et al (2014) [18] | ≥95%  | 21.7 THz         |
| Yang et al (2014) [20]     | >90%  | 37.8 THz         |
| Fan et al (2015) [27]      | ≈100% | 0.24 THz         |
| Ding et al (2015) [21]     | >90%  | 187.5 THz        |
| Liu et al (2015) [29]      | >90%  | 0.6 THz          |
| Zhang et al (2016) [22]    | >99%  | 0.01 THz         |
| Sui et al (2016) [24]      | ≈100% | single frequency |
| Mo et al (2016) [23]       | 80%   | single frequency |
| Yu et al (2016) [25]       | >90%  | 0.55 THz         |
| Our Polarization Converter | >90%  | 0.453 THz        |

symmetry of the designed micro-structure. In addition, another innovation point is that the physical mechanism of polarization conversion (of our designed device) results from field-suppression of co-polarization components and field-enhancement of cross-polarization components, respectively, which is quite different from the conventional case of geometry phase [19–23]. In a word, our focusing is the bandwidth tunable and the new physical mechanism of the cross-polarization conversion rather than the high PCR and the broad bandwidth.

## 5. Conclusion

In summary, we have investigated a transmission-mode THz broadband cross-polarization converter by designing single-layer ultrathin metasurfaces embedded with lower-order-symmetry of split dual-ring air slots. By selecting proper design parameters, the bandwidth of such linear polarization converter can be reached to 0.45 THz with PCR over 90%, due to the phase difference of  $\pi$  between the co-polarized electric components and 0 between the cross-polarized electric components. More specifically, we also experimentally demonstrated that the bandwidth with PCR over 90% could be simply modulated by gradually shifting the side metal rods located in the split dual-ring air slots. The cross-polarized converter device presented here may pave the way to use single-layer metasurfaces for the design of ultra-compact and bandwidth-controllable transmission-type of the THz functional devices.

## Acknowledgments

This work is supported in part by the National Program on Key Basic Research Project of China (973 Program, 2014CB339806), the Major National Development Project of Scientific Instrument and Equipment (2017YFF0106300, 2016YFF0100503), National Natural Science Foundation of

China (61722111), the Key Scientific and Technological Project of Science and Technology Commission of Shanghai Municipality (15DZ0500102), Shanghai Leading Talent (2016-019), and Young Yangtse Rive Scholar (Q2016212).

## References

- [1] Ferguson B and Zhang X C 2002 Materials for terahertz science and technology *Nat. Mater.* **1** 26–33
- [2] Siegel P H 2004 Terahertz technology in biology and medicine *IEEE MTT-S Trans. Microw. Theory Tech.* **52** 2438–47
- [3] Stoik C D, Bohm M J and Blackshire J L 2008 Nondestructive evaluation of aircraft composites using transmissive terahertz time domain spectroscopy *Opt. Express* **16** 17039–51
- [4] Piesiewicz R, Jacob M, Schoebel J and Kurner T 2008 Performance analysis of future multigigabit wireless communication system at THz frequencies with highly directive antennas in realistic indoor environments *IEEE J. Sel. Top. Quantum Electron.* **14** 421–30
- [5] Kakimi R, Fujita M, Nagai M, Ashida M and Nagatsuma T 2014 Capture of a terahertz wave in a photonic crystal slab *Nat. Photon.* **8** 657–63
- [6] Yu N F, Genevet P, Kats M A, Aieta F, Tetienne J P, Capasso F and Gaburro Z 2011 Light propagation with phase discontinuities: generalized laws of reflection and refraction *Science* **334** 333–7
- [7] Huang L L, Chen X Z, Muhlenbernd H, Li G X, Bai B F, Tan Q F, Jin G F, Zentgraf T and Zhang S 2012 Dispersionless phase discontinuities for controlling light propagation *Nano Lett.* **12** 5750–5
- [8] Ding X, Monticone F, Zhang K, Zhang L, Gao D, Burokur S N, de Lustrac A, Wu Q, Qiu C W and Alu A 2015 Ultrathin Pancharatnam–Berry metasurface with maximal cross-polarization efficiency *Adv. Mater.* **27** 1195
- [9] Zhang X, Li Q, Tian Z, Yue W, Gu J Q, Zhang S, Han J G and Zhang W L 2013 Broadband terahertz wave deflection based on c-shape complex metamaterials with phase discontinuities *Adv. Mater.* **25** 4567
- [10] Yin X, Ye Z, Rho J, Wang Y and Zhang X 2013 Photonic spin hall effect at metasurfaces *Science* **339** 1045–7
- [11] Chen X, Huang L, Muhlenbernd H, Li G X, Bai B, Tan Q, Jin G, Qiu C W, Zhang S and Zentgraf T 2012 Dual-polarity plasmonic metalens for visible light *Nat. Commun.* **3** 1198
- [12] Yu N F, Aieta F, Genevet P, Kats M A, Gaburro Z and Capasso F 2012 A broadband, background-free quarter-wave plate based on plasmonic metasurfaces *Nano Lett.* **12** 6328–33
- [13] Yue F Y, Wen D D, Xin J T, Gerardot B, Li J S and Chen X 2016 Vector vortex beam generation with a single plasmonic metasurface *ACS Photonics* **3** 1558–63
- [14] Mehmood M Q et al Visible-frequency metasurface for structuring and spatially multiplexing optical vortices *Adv. Mater.* **28** 2533–9
- [15] Ni X, Kildishev A V and Shalaev V M 2013 Metasurface holograms for visible light *Nat. Commun.* **4** 2807
- [16] Hao J, Yuan Y, Ran L, Jiang T, Kong J, Chan C T and Zhou L 2007 Manipulating electromagnetic wave polarizations by anisotropic metamaterials *Phys. Rev. Lett.* **99** 063908
- [17] Li T, Wang S M, Cao J X, Liu H and Zhu S N 2010 Cavity-involved plasmonic metamaterial for optical polarization conversion *Appl. Phys. Lett.* **97** 261113
- [18] Levesque Q, Makhsiyani M, Bouchon P, Pardo F, Jaeck J, Bardou N, Dupuis C, Haidar R and Pelouard J 2014 Plasmonic planar antenna for wideband and efficient linear polarization conversion *Appl. Phys. Lett.* **104** 111105

- [19] Grady N K, Heyes J E, Chowdhury D R, Zeng Y, Retien M T, Azad A K, Taylor A J, Dalvit D A and Chen H T 2013 Terahertz metamaterials for linear polarization conversion and anomalous refraction *Science* **340** 1304–7
- [20] Yang Y, Wang W, Moitra P, Kravchenko I I, Briggs D P and Valentine J 2014 Dielectric meta-reflectarray for broadband linear polarization conversion and optical vortex generation *Nano Lett.* **14** 1394–9
- [21] Ding F, Wang Z, He S, Shalaev V M and Kildishev A V 2015 Broadband high-efficiency half-wave plate: a supercell-based plasmonic metasurface approach *ACS Nano* **9** 4111–9
- [22] Zhang L, Zhou P, Chen H, Lu H, Xie H, Zhang L, Li E, Xie J and Deng L 2016 Ultrabroadband design for linear polarization conversion and asymmetric transmission crossing x- and k-band *Sci. Rep.* **6** 33826
- [23] Mo W, Wei X, Wang K, Li Y and Liu J 2016 Ultrathin flexible terahertz polarization converter based on metasurfaces *Opt. Express* **24** 13621–7
- [24] Sui S, Ma H, Wang J, Feng M, Pang Y, Xia S, Xu Z and Qu S 2016 Symmetry-based coding method and synthesis topology optimization design of ultra-wideband polarization conversion metasurfaces *Appl. Phys. Lett.* **109** 014104
- [25] Yu X, Gao X, Qiao W, Wen L and Yang W 2016 Broadband tunable polarization converter realized by graphene-based metamaterial *IEEE Photonics Tech. Lett.* **28** 2399–402
- [26] Cong L, Cao W, Zhang X, Tian Z, Gu J, Singh R, Han J and Zhang W 2013 A perfect metamaterial polarization rotator *Appl. Phys. Lett.* **103** 171107
- [27] Fan R, Zhou Y, Ren X, Peng R, Jiang S, Xu D, Xiong X, Huang X and Wang M 2015 Freely tunable broadband polarization rotator for terahertz waves *Adv. Mater.* **27** 1201–6
- [28] Wu S, Zhang Z, Zhang Y, Zhang K, Zhou L, Zhang X and Zhu Y 2013 Enhanced rotation of the polarization of a light beam transmitted through a silver film with an array of perforated s-shaped holes *Phys. Rev. Lett.* **110** 207401
- [29] Liu W, Chen S, Li Z, Cheng H, Yu P, Li J and Tian J 2015 Realization of broadband cross-polarization conversion in transmission mode in the terahertz region using a single-layer metasurface *Opt. Lett.* **40** 3185–8
- [30] Wang J, Shen Z, Gao X and Wu W 2015 Cavity-based linear polarizer immune to the polarization direction of an incident plane wave *Opt. Lett.* **41** 424–7
- [31] Roberts A and Lin L 2012 Plasmonic quarter-wave plate *Opt. Lett.* **37** 1820–2
- [32] Gorodetski Y, Lombard E, Drezet A, Genet C and Ebbesen T 2012 A perfect plasmonic quarter-wave plate *Appl. Phys. Lett.* **101** 201103
- [33] Yu N F, Aieta F, Genevet P, Kats M A, Gaburro Z and Capasso F 2012 A broadband, background-free quarter wave plate based on plasmonic metasurfaces *Nano Lett.* **12** 6328–33
- [34] Jiang S, Xiong X, Hu Y, Ma G, Peng R, Sun C and Wang M 2014 Controlling the polarization state of light with a dispersion-free metastructure *Phys. Rev. X* **4** 021026
- [35] Ma H, Wang G, Kong S and Cui T J 2014 Broadband circular and linear polarization conversions realized by thin birefringent reflective metasurfaces *Opt. Mater. Express* **4** 1717–24
- [36] Cong L, Xu N, Gu J, Han J and Zhang W 2014 Highly flexible broadband terahertz metamaterial quarter-wave plate *Laser Photonics Rev.* **8** 4626–32
- [37] Wang D, Gu Y, Gong Y, Qiu C W and Hong M H 2015 An ultrathin terahertz quarter-wave plate using planar babinet-inverted metasurface *Opt. Express* **23** 11114–22
- [38] Strikwerda A C, Fan K, Tao H, Pilon D V, Zhang X and Averitt R D 2008 Comparison of birefringent electric splitting resonator and meanderline structures as quarter-wave plates at terahertz frequencies *Opt. Express* **17** 136–49
- [39] Yang Y, Huang R, Cong L, Zhu Z, Gu J, Tian Z, Singh R, Zhang S, Han J and Zhang W J 2011 Modulating the fundamental inductive-capacitive resonance in asymmetric double-split ring terahertz metamaterials *Appl. Phys. Lett.* **98** 121114
- [40] Schwind M, Kasemo B and Zoric L 2013 Localized propagating plasmons in metal films with nanoholes *Nano Lett.* **13** 1743–50